The Astronomical Journal, 162:14 (19pp), 2021 July https://doi.org/10.3847/1538-3881/abfaff

Precision Millimeter Astrometry of the α Centauri AB System

Rachel Akeson[1], Charles Beichman[2], Pierre Kervella[3], Edward Fomalont[4,5], and G. Fritz Benedict[6]
[1] NASA Exoplanet Science Institute, Caltech-IPAC, Pasadena, CA 91125, USA; rla@ipac.caltech.edu
[2] NASA Exoplanet Science Institute, IPAC, Jet Propulsion Laboratory, California Institute of Technology, Pasadena, CA 91125, USA; chas@ipac.caltech.edu
[3] LESIA, Observatoire de Paris, Université PSL, CNRS, Sorbonne Université, Université de Paris, 5 Place Jules Janssen, F-92195 Meudon, France
pierre.kervella@observatoiredeparis.psl.eu
[4] National Radio Astronomy Observatory, Charlottesville, VA 22903, USA; efomalon@nrao.edu
[5] ALMA, Vitacura, Santiago, Chile
[6] McDonald Observatory, University of Texas, Austin, TX 78712, USA; fritz@astro.as.utexas.edu
Received 2020 October 26; revised 2021 April 20; accepted 2021 April 21; published 2021 June 14

Abstract

Alpha Centauri A is the closest solar-type star to the Sun and offers the best opportunity to find and ultimately to characterize an Earth-sized planet located in its habitable zone. Here, we describe initial results from an Atacama Large Millimeter/submillimeter Array (ALMA) program to search for planets in the α Cen AB system using differential astrometry at millimeter wavelengths. Our initial results include new absolute astrometric measurements of the proper motion, orbital motion and parallax of the α Cen system. These lead to an improved knowledge of the physical properties of both α Cen A and B. Our estimates of ALMA's relative astrometric precision suggest that we will ultimately be sensitive to planets of a few tens of Earth mass in orbits from 1 to 3 au, where stable orbits are thought to exist.

Unified Astronomy Thesaurus concepts: Fundamental parameters of stars (555); Main sequence stars (1000); Radio astrometry (1337); Astrometric binary stars (79)

Supporting material: machine-readable tables

1. Introduction

At a distance of 1.34 pc, α Cen A is an ideal target for exoplanet searches and is 2.7 times closer than the next most favorable G star, τ Ceti. Alpha Cen A's luminosity of 1.5 $L_{\odot}$ (Thévenin et al. 2002) puts the center of its habitable zone (HZ) at a physical separation of 1.2 au, which corresponds to an angular separation of 0.″9. Alpha Cen A is thus an attractive target for direct imaging searches for planets using ground- or space-based observatories (Kasper et al. 2019; Beichman et al. 2020; Wagner et al. 2021). Current precision radial velocity (PRV) observations (Zhao et al. 2018) constrain the mass of any planet to be $M \sin(i) < 53 M_{\oplus}$ in the habitable zone (1.2 au). Examination of their Figure 6, which includes their estimates for the effects of non-Gaussian noise sources ("red noise") suggests a limit between 50 and 100 $M_{\oplus}$. This limit applies to the near edge-on, 79°, orientation of the α Cen AB system, for which dynamical studies indicate the presence of a stable zone $\lesssim$2.8 au (or 2.″1) around α Cen A despite the presence of α Cen B (Quarles & Lissauer 2016; Holman & Wiegert 1999; Quarles et al. 2018; Quarles & Lissauer 2018).

Due to the proximity of the α Cen system, observations by Liseau et al. (2015, 2016) with the Atacama Large Millimeter/submillimeter Array (ALMA) detected both stellar photospheres, allowing a unique opportunity to measure astrometric motion with ALMA. Recently, the first radio astrometric planetary detection was announced by Curiel et al. (2020) with the discovery of a planet around the M dwarf TVLM 51346546 using the Very Long Baseline Array.

In this paper, we present results from an ALMA observing program designed both to test the astrometric capabilities of ALMA and to make initial measurements of the α Cen AB system. Section 2 describes our ALMA observations, data reduction, astrometric measurements and the contribution of stellar activity to the astrometric noise. Section 3 includes our determination of the orbital and physical parameters for α Cen A and B, combining our new data with previous observations, and a discussion of future prospects for planet detection. Our conclusions are given in Section 4, and Appendix A provides the ephemeris of α Cen A and B.

2. Astrometry with ALMA

2.1. Observations

The properties of α Cen A and B are well known from previous observations. At submillimeter wavelengths, the stellar fluxes range from 10 to 100 mJy (Liseau et al. 2016), the angular sizes are 8.5 and 6.0 mas (Kervella et al. 2017a), the orbital separation ranges from 2″ to 21″ and the short-term motion on the sky is 0.8 mas per hour. From these parameters and looking to balance the signal-to-noise ratio (SNR), the angular resolution and the field of view, we chose to observe in band 7. As the astrometric precision scales directly with the angular resolution, observations when ALMA is in configurations with maximum baselines of 2 km or larger are most desirable, which limits the time sampling. Hence, observations were requested in three configurations, one in Fall 2018 and two in Summer 2019. We obtained a series of ALMA observations of α Cen in Cycle 6 between 2018 October and 2019 August at band 7, using the nominal continuum set-up of four 1.9 GHz spectral windows at frequencies 336.5, 338.5, 348.5, and 350.5 GHz (Table 1). To keep both sources well within the primary beam, we placed the phase center for each 70 minute observation at the center of mass of α Cen A and B.

To assist in the determination of systematics in the astrometric measurements, we designed the observations with two levels of repetition. Within a configuration, we requested two observation blocks separated by up to 14 days. Within an observation block, we executed two independently calibrated

Table 1
ALMA Observation Log

Observation Pair Dates	Maximum Baseline (km)	Beam (mas)	Rms (μJy)	A int. Flux[a] (mJy)	B int. Flux[a] (mJy)
2018 Oct 14[b]	2.5	160×83	38	20.77 ± 0.15	9.07 ± 0.15
2019 Jul 15–16	8.5	40×25	27	22.34 ± 0.058	9.71 ± 0.055
2019 Jul 19–20	8.5	35×21	30	21.19 ± 0.081	9.83 ± 0.081
2019 Aug 12–13	3.6	68×57	49	22.60 ± 0.066	10.59 ± 0.065
2019 Aug 25–26	3.6	69×55	50	26.08 ± 0.051	11.91 ± 0.051

Notes.
[a] Integrated flux uncertainty from fit; does not include absolute flux error
[b] Only one observation block observed in this configuration

observations, with little or no time gap in between them. In 2018 October, we obtained only a single observational block, and one of the two observations within this block has issues (see Section 2.2.1) and is not included in the astrometric data results. Thus, our final observation set includes nine calibrated observations from five blocks: one block in configuration 6 (max baseline 2.5 km), two blocks in configuration 8 (max baseline 8 km), and two blocks in configuration 7 (max baseline 3.6 km).

Each observation block consisted of the following: (1) the standard on-line calibrations: pointing, delay offset, and system temperature of each antenna; (2) a 2 minute scan at the beginning of each observation of the bright quasar, J1427–4206, with a known flux density; (3) the main science target portion of the observation of about 55 observing cycles, each with an 18 s scan on the phase calibrator J1452–6502, alternating with a 50 s scan on α Cen; (4) within the science portion, five of the α Cen target integrations were replaced by a check source, J1424–6807.

2.2. Data Reduction

We used the standard ALMA data calibration for all observations. The amplitude calibration for each antenna/spectral-window channel was determined from the 2 minute scan of J1427–4206 and applied to the rest of the observation. The measured antenna/spectral-window scale factor is constant within 5% over the ~hour observation duration. The phase difference between each antenna/spectral-window antenna or spectral window was essentially constant, and was also obtained from the 2 minute scan and applied to the entire observation. Thus, the eight data channels (four spectral windows times two polarizations) could be combined to give high SNR for the imaging, self-calibration, and position determinations. The phase calibration for α Cen and the check source was obtained in the normal phase referencing method from the antenna-based phase from each of the fifty 18 s scans on J1452–6502. Alpha Cen and the check source field were then calibrated using the average of the antenna-based phase of J1452–6502 just before and after the relevant scan.

To provide an independent check of the absolute accuracy of these observations, we included five 20 s scans of the quasar J1424–6807 near α Cen in each epoch as a check source. This quasar is in the International VLBI Service for Geodesy and Astrometry list, and has a celestial position accuracy <0.5 mas. Except for the integration time, which was about 3.5% of that of α Cen, the identical check source observation and analysis methods provide an independent confirmation of the absolute precision of the ALMA results.

From this calibrated data, we used the *tclean* program from the *casa* software package (McMullin et al. 2007) to produce images for each of the calibrated observations, using the nominal data weighting (weighting = briggs, robust = 0). The image size of 2048×2048 pixels, with grid separation 5 mas, covered nearly all of the ALMA primary beam. The clean deconvolution algorithm removed the point-spread function associated with the spatial frequency (*uv*) coverage of the observation. The image resolution varied from 20 mas to 150 mas, depending on the configuration. We derived all astrometric positions from the images; we did not use *uv* data analysis to obtain the source positions. Using the stellar radii and parallax from Kervella et al. (2017a), the angular diameters of α Cen A and B are 8.5 and 6.0 mas, respectively. Thus, the individual photospheres are not resolved in these observations. For the J1424–6807 check source, we analyzed an image size of 512×512 pixels.

The flux for α Cen A and B for each epoch is given in Table 1. The integrated flux was determined using the *casa* routine *imfit* to fit a Gaussian to each star. The uncertainty reported is the fitting uncertainty and does not include the absolute flux error. As the focus of these observations was astrometry, no primary flux calibration standards were observed; thus, the absolute calibration uncertainty is 10–15%. Within this absolute uncertainty, our fluxes agree with those of Liseau et al. (2016).

2.2.1. Absolute Astrometry

The images made for each one-hour observation of α Cen A and B are on the Very Long Baseline Interferometer (VLBI) J2000.0 International Celestial Reference System (ICRS) because the phase reference calibrator, J1452–6502, and other interferometric parameters used for these ALMA calibrations and reductions are on this frame associated with very distant quasars. The measured positions from each one-hour observation of α Cen A and B are shown in Table 2, as measured using the *casa* routine *jmfit*. The positional change of each science target star due to proper motion and parallax is less than 1 mas in one hour. Each hour-long observation can be combined into an average position with no significant loss of precision in the absolute position.

We obtain a further check of the experimental accuracy from an analysis of the image position and stability of the check source J1424–6807. For the four highest-resolution observations with a beam of about 30 mas taken in 2019 July, the average offset of the check source between our measured ALMA position and its ICRS position is about 2.5 mas. This displacement varied somewhat with the quality and variability

Table 2
Measured Positions in IRCS

Date	Start Time (UT hr)	Star	R.A. (deg)	Decl. (deg)	$\sigma_{\text{R.A.}}$ cos(decl.)[a] (arcsec)	$\sigma_{\text{decl.}}$ (arcsec)
2018 Oct 14	13:38:19.0	A	219.860763250	−60.832171539	0.0039	0.0035
		B	219.859663542	−60.830951061	0.0040	0.0039
2019 Jul 15	23:14:41.3	A	219.858859933	−60.832264944	0.0007	0.0010
		B	219.857984904	−60.830881649	0.0007	0.0010
2019 Jul 16	01:15:31.1	A	219.858854542	−60.832262378	0.0019	0.0014
		B	219.857979000	−60.830879128	0.0018	0.0013
2019 Jul 19	23:31:14.5	A	219.858829571	−60.832252293	0.0004	0.0007
		B	219.857957646	−60.830866720	0.0004	0.0007
2019 Jul 20	01:02:29.9	A	219.858827083	−60.832253354	0.0005	0.0005
		B	219.857955246	−60.830867652	0.0006	0.0007
2019 Aug 12	23:10:35.2	A	219.858667583	−60.832185858	0.0068	0.0057
		B	219.857814792	−60.830785642	0.0071	0.0061
2019 Aug 13	00:44:57.6	A	219.858669208	−60.832186997	0.0049	0.0037
		B	219.857817458	−60.830787197	0.0047	0.0035
2019 Aug 25	23:33:45.5	A	219.858615833	−60.832153722	0.0035	0.0020
		B	219.857773917	−60.830746378	0.0043	0.0024
2019 Aug 26	20:07:30.6	A	219.858613375	−60.832152358	0.0016	0.0016
		B	219.857772625	−60.830744378	0.0018	0.0018

Note.
[a] The rms values given in the table are the internal measurement uncertainties.

of the atmospheric phase stability over each observation. We note that the angular separation between the check source and the phase calibrator is 4.°1, similar to the 4.°5 between α Cen and the phase calibrator. Extrapolating the absolute astrometric accuracy between the check source and α Cen requires scaling with the peak SNR for each source. The check source is roughly two times brighter than α Cen B, but with only 3.5% of the integration time, J1424–6807 will have a noise level $\sqrt{(29)}$ higher. Thus, the SNR ratio between α Cen B and J1424–6807 is a factor of $\sim$3. In the absence of systematics, the best performance on α Cen would scale to $\sim$0.8 mas. As seen in Table 2, the internal uncertainty for the best observation in 2019 July matches this performance. The final absolute astrometric uncertainty will also include contributions from uncorrected phase noise in the α Cen data. Based on variations in the absolute position of A and B using different calibrations and array sizes, we use a conservative value of 3 mas for the absolute astrometric uncertainty for the higher-resolution configurations (2019 July and August) and 6 mas for the lower-resolution data (2018 October) when fitting the orbital parameters in Section 3.1. Future ALMA observations with good phase calibration on long baselines could provide improved absolute astrometric accuracy of $<$1 mas, with internal uncertainties of 0.1–0.2 mas in band 7.

An additional estimate of the absolute position accuracy of α Cen A and B can be obtained by the position difference between each of the five observation pairs in the experiment. Table 3 shows the R.A. and decl. differences between the two position measurements in each pair, after correction for the proper motion. The R.A. Meas column gives the measured difference between the two observations separated by approximately one hour, and the R.A. Err column gives the uncertainty extrapolated from the image fitting errors given in Table 2. Similar entries are given for the decl. measures. The measured differences are correlated with the tropospheric stability during the observation. The measured position differences between the observation pair positions are generally a factor of 3 larger than

Table 3
Absolute Position Difference of Star A for Five Observation Pairs

Avg Date (yr)	R.A. Meas (mas)	R.A. Err cos(decl.) (mas)	Decl. Meas (mas)	Decl. Err (mas)
2018.7853	−6.6	3.3	28.2	3.0
2019.5371	6.1	1.0	−6.1	1.0
2019.5480	2.3	0.4	2.5	0.6
2019.6138	−0.7	1.4	3.1	1.0
2019.6505	−2.7	2.2	3.7	1.3

that expected from the internal position error based on the fitting of the star on each image alone. A similar scaling is obtained for α Cen B, which is not shown. The one anomaly is for the observation on 2018 October 14 at 15.1 hr, where the declinations of both stars A and B disagree between the observation pairs on 2018 October 14 at 13.6 hr. This observation is discussed further below. For the second observation block in 2018 October, both α Cen A and B had an unexpected offset of 20 mas, while the check source position repeatability error was less than 4 mas. We continue to investigate this problem, and believe it was caused by an error in the ALMA celestial position tracking system of α Cen. Hence, this observation is not used in our analysis below.

2.2.2. Differential Astrometry

The angular separation between α Cen A and B can be measured from the image for each of the observation epochs. Although the image quality and absolute position offsets may differ, the atmospheric distortions act nearly identically on α Cen A and B. Thus, their angular separation is nearly independent of the quality of the image, but with an error consistent with the SNR of each star. An empirical relationship (Monet et al. 2010) shows the dependence of astrometric precision, σ, on the full width at half maximum, FWHM, of the

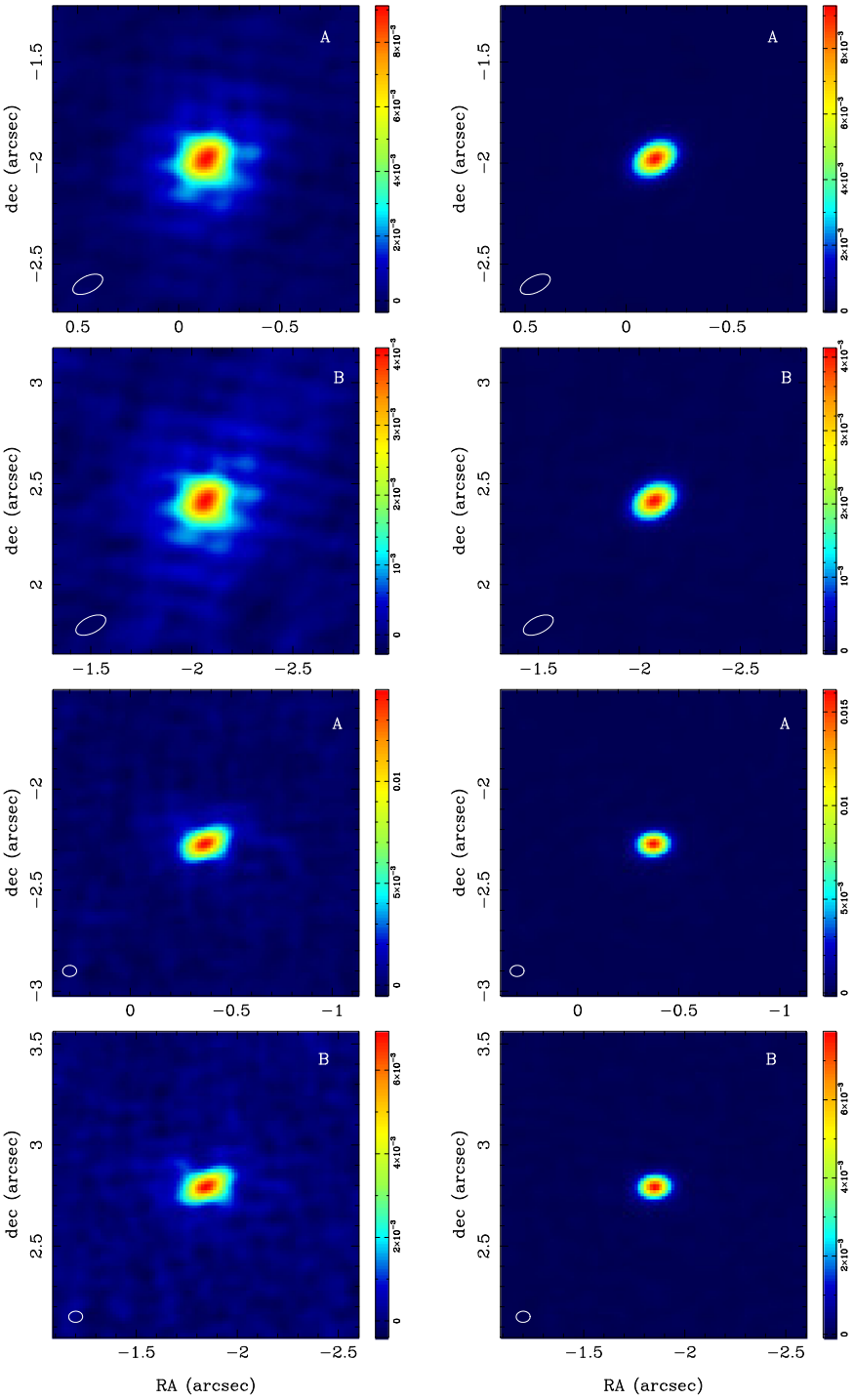

Figure 1. Images of α Cen A and B from 2018 October 14 (top four panels) and 2019 August 15 (bottom four panels). Images on the left show standard phase calibration, and images on the right show the corresponding data after phase self-calibration. Each image is scaled independently to show the noise reduction after self-calibration. The standard phase calibration images clearly show a larger size at the 10% flux level due to smearing from uncorrected phase noise.

beam and SNR of the signal: $\sigma \sim \mathrm{FWHM}/(2 \times \mathrm{SNR})$. Our results are consistent with this expectation.

As the radio emission from the two stars is sufficiently bright and compact, we self-calibrate the α Cen data in order to remove most of the residual tropospheric phase errors (Schwab 1980). We used the self-calibration algorithm to improve the α Cen image quality, and the following paragraph describes how the initial model for α Cen assumed for self-calibration makes no significant difference to the A–B angular separation. Figure 1 shows an image of α Cen A and B before and after phase self-calibration, compared with an image obtained with only normal phase referencing, for two observations with different spatial resolutions. The improvement in the image quality is shown by the SNR, which increases by factor of $\sim$2 and by the significantly lower residuals. Except for the emission from the two stars, we find no emission in the field of view greater than 0.3% of the emission from α Cen A.

Table 4
Relative Position of α Cen B with Respect to A from ALMA

Date (UT)	Time (UT) (hr)	Decimal year	E–W Separation cos(decl.) (arcsec)	σ_{E-W} cos(decl.) (arcsec)	N–S separation (arcsec)	σ_{N-S} (arcsec)
2018 Oct 14	13.6	2018.78520	−1.9310	0.0004	−4.3952	0.0003
2019 Jul 15	23.2	2019.53697	−1.5355	0.0003	−4.9799	0.0003
2019 Jul 16	01.3	2019.53720	−1.5361	0.0005	−4.9802	0.0003
2019 Jul 19	23.5	2019.54796	−1.5295	0.0003	−4.9884	0.0003
2019 Jul 20	01.0	2019.54813	−1.5297	0.0003	−4.9884	0.0003
2019 Aug 12	23.5	2019.61366	−1.4953	0.0003	−5.0392	0.0003
2019 Aug 13	01.0	2019.61385	−1.4945	0.0003	−5.0390	0.0003
2019 Aug 25	23.6	2019.64934	−1.4761	0.0005	−5.0662	0.0003
2019 Aug 26	20.1	2019.65168	−1.4751	0.0003	−5.0684	0.0003

Because we obtain significantly improved image quality with self-calibration (Figure 1), the α Cen A to B separations measured from those images also have higher precision and accuracy. To check the impact of the self-calibration, the A-to-B separation was measured for three cases: (1) no self-calibration, (2) self-calibration for A only, and (3) self-calibration for A and B. The separations for these three methods agreed to within the uncertainties, and Table 4 contains α Cen A-to-B separations measured from self-calibrated images for both sources. The angular separation and estimated error (using the casa routine *jmfit*) are given in Table 4, measured using self-calibration method (3). The uncertainties in total separation are from the positional fitting and range from 0.3 to 0.6 mas. As absolute position information is not preserved during self-calibration; these data are only used for the A-to-B separation, not for the absolute positions given in Table 2.

2.3. Astrometric Noise due to Stellar Activity

Dumusque (2018) discusses the effects of stellar variability in the context of PRV for planet detection, where changes in the shapes of spectral lines formed at different heights in stellar photospheres and chromospheres can adversely impact radial velocity precision at the $\sim$1 m s^{-1} level even for quiescent stars. A similar effect introduces spurious signals in astrometric observations. Time-variable spatial inhomogeneities on the surfaces of stars produce variations in their astrometric positions (Makarov et al. 2009). In the astrometric case, the causes of the variability include surface features such as sunspots and active regions, which may appear as fainter or brighter than the surrounding photosphere depending on wavelength. As spots rotate across and then behind the face of the star, the intensity-weighted centroid of the stellar disk will shift.

Appropriate to their age, both α Cen stars are relatively quiescent with an activity index $R'HK = -5.15$ and -4.97 for A and B, respectively (Boro Saikia et al. 2018; Lisogorskyi et al. 2019). Spectroscopic studies and X-ray data (Robrade & Schmitt 2016) show α Cen B to be modestly more active than α Cen A, but both are similar in their activity levels to the Sun (Mamajek & Hillenbrand 2008). Alpha Cen B is brighter at X-ray wavelengths (Robrade & Schmitt 2016) and shows a stronger chromospheric component (Trigilio et al. 2018). Both stars show cyclical variations in X-ray brightness over an almost 20 yr span (Robrade & Schmitt 2016).

Alpha Cen A and B are strong sources at millimeter and submillimeter wavelengths. The spectral energy distribution in Figure 2 spans observations from the Spitzer, Herschel, ALMA, and the Australia Telescope Compact Array (ATCA) observatories, as tabulated in Liseau et al. (2013) and Trigilio et al. (2018) using ALMA values as updated with an improved calibration model (Liseau 2019). To assess the possible impact of variability in the positions of the two stars, we first must determine the dominant source of emission at our ALMA wavelength (band 7; 343 GHz or 874 μm). For α Cen A, we fitted the absolute flux densities for a $T_{\rm eff} = 5800$ K BT-Settl model (Baraffe et al. 2015) using $R_* = 1.22\ R_\odot$ at 1.334 pc (Kervella et al. 2017a) to the visible and near-infrared data listed in SIMBAD and Engels et al. (1981). The fitted "photospheric" component is shown as the red-dashed curve in Figure 2 and has a normalization uncertainty of 9% (1σ). To account for the excess obvious at longer wavelengths, we combine the photospheric emission with a simplified representation of free–free chromospheric emission following Mezger & Henderson (1967) with an optical depth given by:

$$\tau = 3.28 \times 10^{-7}\left(\frac{T_{\rm gas}}{10^4\ {\rm K}}\right)^{-1.35} \nu^{-2.1} \times {\rm EM}$$

and the corresponding flux density

$$F\nu = \frac{2k_{\rm B}T\nu^2}{c^2}\Omega(1 - e^{-\tau}),$$

where τ is the free–free optical depth, $T_{\rm gas}$ is the temperature of the ionized gas, ν the frequency, EM the Emission Measure in pc cm^{-6}, $k_{\rm B}$ is the Boltzmann constant, and Ω the solid angle of the star.

We fit the free–free emission from α Cen A with a two-parameter model, solving for gas temperature, $T_{\rm gas}$, and emission measure, EM. The combination of photosphere (red-dashed line in Figure 2) and free–free (blue-dashed line) emission provides a good fit to the data (solid black line) with $T_{\rm gas} = 5100 \pm 650$ K and ${\rm EM} = 3.0 \pm 0.4 \times 10^{10}$ pc cm^{-6}. The derived $T_{\rm gas}$ and EM (which corresponds to a 500–1000 km emitting region with an electron density of $\sim 3 \times 10^{10}$ cm^{-3}) are comparable to the values in Trigilio et al. (2018).

The fit has a χ^2 value of 62 with 24 degrees of freedom. The high value of χ^2 may be related to either variability in the multiple epochs of submillimeter data or to an underestimate of the absolute calibration of the data. We estimate the fractional contributions of the photosphere and chromosphere, Φ_p and Φ_c, respectively, using the combined photospheric versus chromospheric model for band 7. A Monte Carlo simulation varying T_C, EM, and the photospheric normalization, 1.02 ± 0.09, relative to their uncertainties gives a photospheric fraction of $\Phi_p = 85\% \pm 1.3\%$ versus chromospheric fraction

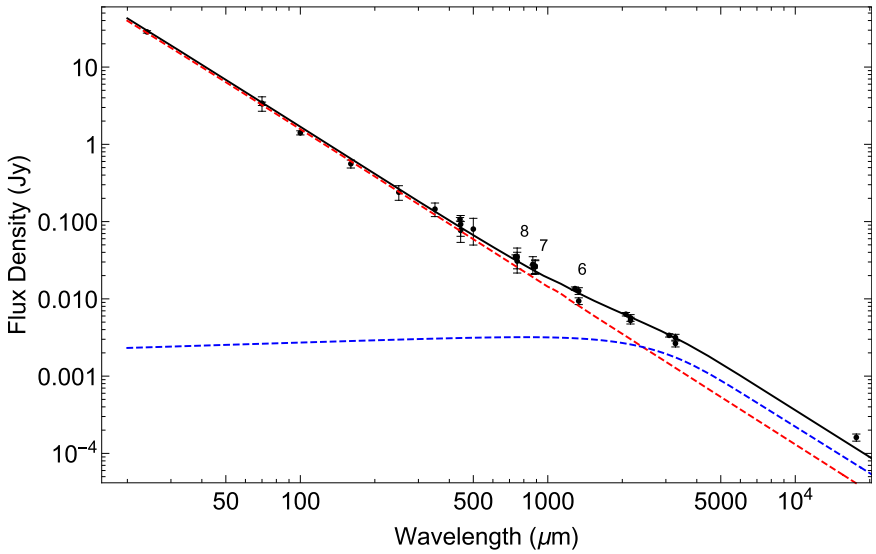

Figure 2. A combination of Rayleigh–Jeans photospheric emission (red-dashed line) plus a free–free emission spectrum (blue-dashed line) is fitted to photometry of α Cen A. ALMA bands 6, 7, and 8 are indicated.

$\Phi_c = 1 - \Phi_p = 15\% \pm 1.4\%$. We performed a similar fit to the data for α Cen B ($T_{\rm eff} = 5300$ K) and derived $\Phi_p = 69\% \pm 7\%$ and $\Phi_c = 31\% \pm 7\%$ chromospheric.

We are now in a position to assess the potential variability of the α Cen stars. A detailed analysis (Makarov et al. 2009) suggests that a quiescent star like the Sun would have a photospheric jitter at visible wavelengths of 1 μau or 0.75 μas at distance of 1.34 pc. Their model was based on an evolving population of sunspots on a rotating star with the starspots having an average temperature of $T_{\rm spot} \sim 4000$ K versus a photospheric temperature of $T_{\rm phot} \sim 5800$ K. At 0.55 μm the difference in surface brightness between these two regions would be $B_\nu(T_{\rm spot},\ 0.55\ \mu{\rm m})/B_\nu(T_{\rm phot},\ 0.55\ \mu{\rm m}) = 0.13$, whereas in band 7 (874 μm) the contrast would be much more muted, $B_\nu(T_{\rm spot},\ 874\ \mu{\rm m})/B_\nu(T_{\rm phot},\ 874\ \mu{\rm m}) = 0.69$, where B_ν is the Planck function. Thus, a contrast-driven spatial jitter due to starspots in α Cen A would be smaller by $0.69/0.13 = 5.3$, or only $\sigma_{\rm phot} = 0.14$ μas in the submillimeter. Unless α Cen A or B is unusually active, which is not indicated by their $R'HK$ values, the purely photospheric contribution to astrometric jitter will be negligible.

We must still take into account any jitter in the free–free emission, which comprises perhaps 15% of the total emission from α Cen A in band 7. To assess this source of spatial variability we draw on a series of 17 GHz maps of the Sun obtained with 5″ resolution taken daily by the Nobeyama Radio Interferometer (Shibasaki 2013). Illustrative maps around Solar Maximum (2001) and Solar Minimum (2010) are shown in Figure 3(a) and (b). We evaluated the shift between the intensity-weighted centroid and the nominal disk center by calculating the centroid of all chords across the solar disk in both the vertical and horizontal directions. We made this calculation for every day within 2001 (Solar Maximum) and 2010 (Solar Minimum) for which there were maps of suitable quality (244 in 2001 and 300 in 2010). Maps were subjected to visual examination to reject obvious artifacts.

Figure 3 shows the combined histogram of day-to-day shifts in the x and y centroids with a 1σ standard deviation of 6.″46, or $\sigma_{\odot,{\rm active}} = 0.36\%$ of the solar disk during 2001, and less than half that amount, 2.″64 or $\sigma_{\odot,{\rm quiet}} = 0.15\%$ in 2010 (Table 5). Multiplying these centroid shifts by the angular diameters of α Cen A and B, $\theta_{\rm A,B}$ (Kervella et al. 2017a), gives estimates of the jitter arising in the chromosphere, $\sigma_c = \sigma_\odot \theta$, expected from each star in active or quiescent phases.

However, the influence of the chromospheric jitter term on the ALMA measurement is reduced by the contribution of the chromospheric emission to the total, $\Phi_c = 32\% \pm 13\%$. Propagating the Monte Carlo simulation of the photospheric versus chromospheric faction into the jitter calculation yields the net amount of jitter expected for the two stars separately for the active and quiet states (Table 5). These terms dominate the purely photospheric component due to starspots.

Finally, the astrometric jitter in the measurement of the separation between the two stars is given by the rms sum of estimates for the two stars separately, $\sigma_{\rm tot} = \Phi_c \sqrt{\sigma_{c,{\rm A}}^2 + \sigma_{c,{\rm B}}^2}$, and varies between 15 and 6 μas in the active and quiet Sun cases. This value represents only an order of magnitude estimate but suggests that for the purposes of astrometrically detecting planets significantly more massive than the Earth, stellar jitter terms are likely to be negligible in comparison with instrumental terms.

3. Results

3.1. Orbital and Physical Parameters of α Cen A and B

Our ALMA observations have particular value for the determination of the orbit and proper motion of the α Cen AB system. They are both the first precision absolute astrometric measurements of the positions of the two stars (referenced to the quasar frame) since Hipparcos, and the highest accuracy differential astrometric positions available to date. Due to the brightness and binarity of α Cen AB, Gaia standard processing is unavailable and custom data reductions may be limited in absolute accuracy. However, the third component of the system, Proxima (Kervella et al. 2017b), is measured by Gaia with a high accuracy (Benedict & McArthur 2020; Kervella et al. 2020). Our analysis includes thousands of radial velocity (RV) measurements of both components. The constraint provided by the requirement that astrometry and RV describe the same physical system improves the accuracy of our results.

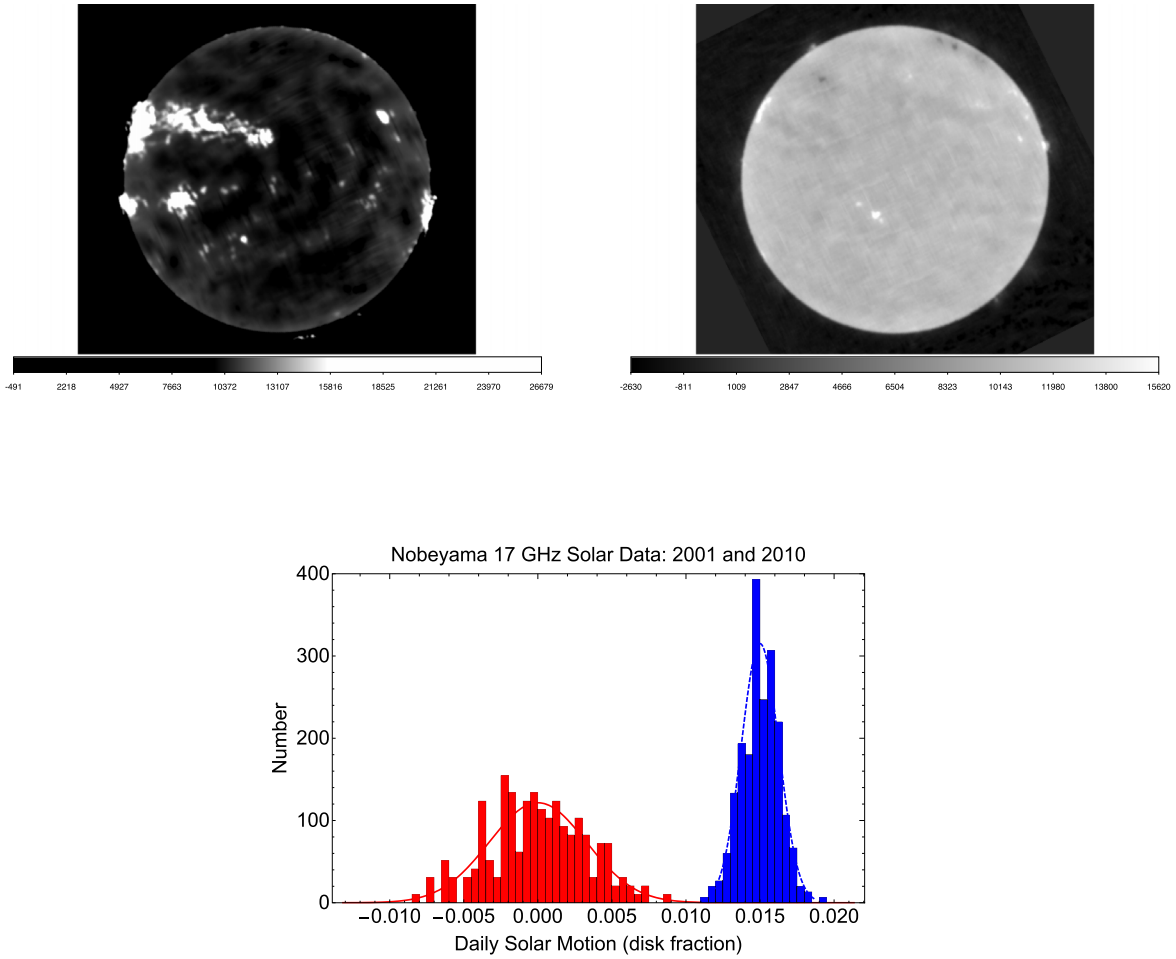

Figure 3. Top: solar images from 2001 (left, Solar Maximum) and 2010 (right, Solar Minimum) at 17 GHz from the Nobeyama telescope. Units are of brightness temperature, with quiescent regions having values around 10^4 K. Bottom: histograms showing the number of days with varying amounts of offsets in the intensity-weighted centroid of the daily 17 GHz maps in 2001 (left, Solar Maximum in red) and 2010 (right, Solar Minimum in blue and displaced by 0.15 for clarity). Units are in fractions of the solar disk diameter. The 1σ jitter in the centroid is $\sigma_{\odot} = 0.36\%$ (active) and $\sigma_{\odot} = 0.15\%$ (quiet). Gaussian distributions are overplotted on the histograms.

Table 5
Estimates of Astrometric Jitter

Quantity	α Cen A	α Cen B
Active solar jitter (disk fraction), $\sigma_{\odot,\mathrm{active}}$	0.36%	
Quiet solar jitter (disk fraction), $\sigma_{\odot,\mathrm{quiet}}$	0.15%	
Chromospheric fraction, Φ_c	$15\% \pm 1.4\%$	$36\% \pm 7\%$
Stellar diameter, $\theta_{\mathrm{A,B}}$ (mas)[a]	8.5	6.0
Stellar jitter (active, μas), $\sigma_{\mathrm{c,active}}$	4.6	8.5
Stellar jitter (quiet, μas), $\sigma_{\mathrm{c,quiet}}$	1.9	3.5
Total jitter (active, μas), $\sigma_{\mathrm{tot,active}}$	15 ± 10	
Total jitter (quiet, μas), $\sigma_{\mathrm{tot,quiet}}$	6 ± 4	

Note.
[a] Kervella et al. (2017a).

3.1.1. Astrometry Data

To determine the orbital parameters of the system, we included archival *differential* astrometry of the AB pair (Hartkopf et al. 2001) starting in the year 1940 (one full 80 yr orbit as of the year 2020). Measurements older than 1940 do not significantly improve the orbital parameters, due to their larger uncertainties and possible systematics. Our complete astrometric data set includes a Hipparcos measurement (from the data reprocessed by van Leeuwen 2007) combined with the new ALMA data points (Table 4) and these archival data. The complete set of differential measurements, including our new ALMA data, is given in Table 6.

The only available high-accuracy *absolute* astrometric measurements of α Cen A and B are the Hipparcos data and our new ALMA data points from 2018 and 2019. Our complete sample of absolute astrometric measurements includes a total of 10 points; 9 from our ALMA data as given in Table 2 and 1 from Hipparcos (van Leeuwen 2007) UT=1991-04-02T13:30:00.000, $\mathrm{R.A._A} = 219.92040813 \pm 0.00307$, $\mathrm{decl._A} = -60.83514522 \pm 0.00246$, $\mathrm{R.A._B} = 219.91412460 \pm 0.01915$, $\mathrm{decl._B} = -60.83948046 \pm 0.01424$. We assign a systematic uncertainty of $\sigma = 3$ mas to each absolute ALMA astrometric measurement, except for the lower-resolution measurement from 2018 October, which is assigned an uncertainty of 6 mas. These measurements determine the barycentric proper motion. Previous ALMA observations of α Cen from Liseau et al. (2015, 2016) were designed for accurate flux measurements but not for accurate astrometric measurements and are not included in our analysis. In particular, the angular resolution is a factor of several worse than our highest resolution, and cross checks using a check source or between adjacent observations

Table 6
Relative Astrometry of α Cen B with Respect to A

Date (UT) (decimal yr)	Position Angle (deg)	Pos. Angle unc. (deg)	Separation (arcsec)	Separation unc. (arcsec)	Reference
2019.6505	343.7729	0.0032	5.27869	0.00030	this paper
2019.6481	343.7560	0.0053	5.27686	0.00032	this paper
2019.6127	343.4803	0.0033	5.25595	0.00030	this paper
2019.6125	343.4726	0.0033	5.25637	0.00030	this paper
2019.5470	342.9519	0.0033	5.21767	0.00030	this paper
2019.5468	342.9539	0.0033	5.21761	0.00031	this paper
2019.5361	342.8581	0.0053	5.21172	0.00032	this paper
2019.5358	342.8634	0.0033	5.21125	0.00030	this paper
2018.7846	336.2542	0.0089	4.80434	0.00056	this paper
2016.1893	305.19	0.30	4.013	0.02	K16
2015.3326	293.30	0.60	4.020	0.04	K16/ALMA
2014.9574	288.28	0.70	4.081	0.05	K16/ALMA
2014.5426	282.91	0.30	4.208	0.02	K16/ALMA
2014.5126	282.84	0.30	4.184	0.02	K16/ALMA
2014.2410	279.20	0.30	4.330	0.05	An15
2012.7100	262.70	0.40	5.050	0.05	An14
…					

References. K16: Kervella et al. (2016); K16/ALMA: Kervella et al. (2016) measurements of data from Liseau et al. (2015); An15: Anton (2015); An14: Anton (2014).

(This table is available in its entirety in machine-readable form.)

are not possible with those observations. We do, however, use these data as part of the differential astrometric data.

3.1.2. Radial Velocity Data

We adopted RV data from the large series of HARPS measurements of α Cen A and B obtained since 2004, publicly available from the ESO archive. We tested incorporating additional radial velocity measurements from other spectrographs (in particular CES and UVES). However, the shifts in the RV zero-point between these instruments result in additional variables in the orbital fit that degrade the quality and reliability. The extended time coverage provided by these instruments does not compensate for this drawback, and we therefore rely on the homogeneous set of HARPS measurements.

As noted by Lisogorskyi et al. (2019), a significant fraction of the spectra collected for α Cen A were processed using an incorrect cross-correlation mask of type K1V (corresponding in fact to α Cen B). We adopted the α Cen B RV from these authors, rejecting the points with the wrong masks from our sample. We also rejected the high-cadence observations of 2013, known to be affected by a significant intranight drift and possible systematics. The RV data of α Cen A are from the standard ESO pipeline. We could not recompute the α Cen A RV from the raw HARPS data, using a correct spectral-type mask and the standard ESO pipeline, because that pipeline is not publicly accessible.

We corrected the RV shift caused by the HARPS fiber exchange in 2015, as recommended by Trifonov et al. (2020). The applied shift is $\Delta V_A = +13.33$ m s^{-1} and $\Delta V_B = +11.53$ m s^{-1}, which we subtract from the pipeline RVs for epochs later than JD = 2457163. We then filtered out the RV measurements whose uncertainty is larger than 10 m s^{-1}, and cleaned the strongest outliers with a 5σ clipping with respect to the best-fit preliminary solution. The latter step rejects only 0.9% of the measurements of A and 1.0% of B. Our final sample of RV measurements includes 5184 RV measurements for A and 12,383 for B. A sample of the radial velocity data are shown in Table 7, and the complete table is available online. Finally, we checked that adopting the Trifonov et al. (2020) RV shift does not result in a significant change of the final orbital parameters.

Table 7
Radial Velocity Measurements for α Cen A and B from the HARPS Instrument

MJD (days)	Star	Radial Vel. (km s^{-1})	Rad. Vel. σ (km s^{-1})
53039.36288	A	−22.73789	0.00201
53039.36333	A	−22.73742	0.00201
53039.36376	A	−22.73696	0.00202
53139.06947	A	−22.70210	0.00200
53139.07017	A	−22.70149	0.00200
…			

(This table is available in its entirety in machine-readable form.)

Although the statistical uncertainties of the HARPS RV measurements are extremely small (a few times 10 cm s^{-1}), the effective jitter is significantly larger due to stellar activity, cross talk between the two stars, or instrumental effects for these extremely bright targets. Therefore, we added in quadrature a uniform uncertainty of 2 m s^{-1} to all measurements. Following Pourbaix & Boffin (2016; see also Pourbaix et al. 2002; Kervella et al. 2016), we subtracted a constant velocity shift of $V_B = 314$ m s^{-1} from the RV measurements of α Cen B, thereby accounting for its relative gravitational redshift and convective shift with respect to α Cen A, whose intrinsic shift is assumed to be zero.

3.1.3. Orbital and Proper Motion Fit Procedure

To fit the orbital parameters and proper motion, we generally followed the same approach as Kervella et al. (2016). We first

Table 8
Orbital Elements, Masses, Parallax, Position, and Proper Motion of α Cen AB, for Epoch 2019.5

Parameter		Present work	K16	PB16
Semimajor axis (arcsec)	a	17.4930 ± 0.0096	17.592 ± 0.013	17.66 ± 0.026
Inclination (deg)	i	79.2430 ± 0.0089	79.320 ± 0.011	79.32 ± 0.044
Arg. of periastron (deg)	ω	231.519 ± 0.027	232.006 ± 0.051	232.3 ± 0.11
Long. of asc. node (deg)	Ω	205.073 ± 0.025	205.064 ± 0.033	204.85 ± 0.084
Period (yr)	P	79.762 ± 0.019	79.929 ± 0.013	79.91 ± 0.013
Ref. epoch	T_0	1955.564 ± 0.015	1955.604 ± 0.013	1955.66 ± 0.014
Eccentricity	e	0.51947 ± 0.00015	0.5208 ± 0.0011	0.524 ± 0.0011
Barycentric RV (km s^{-1})	V_0	-22.3796 ± 0.0020	-22.3930 ± 0.0043	-22.390 ± 0.0042
RV accel. (m s^{-1} yr^{-1})	$\dot{V}_0$	$+0.421$	...	...
Parallax (mas)	ϖ	750.81 ± 0.38	747.17 ± 0.61	743 ± 1.3
Parallax var. (μas yr^{-1})	$\dot{\varpi}$	$+13.0$	...	...
Mass fraction	$\frac{m_A}{m_A+m_B}$	0.54266 ± 0.00011	0.54116 ± 0.00027	0.5383 ± 0.00044
Mass of A ($M_\odot$)	m_A	1.0788 ± 0.0029	1.1055 ± 0.0039	1.133 ± 0.0050
Mass of B ($M_\odot$)	m_B	0.9092 ± 0.0025	0.9373 ± 0.0033	0.972 ± 0.0045
Radius of A ($R_\odot$)	R_A	1.2175 ± 0.0055		
Radius of B ($R_\odot$)	R_B	0.8591 ± 0.0036		
Luminosity of A ($L_\odot$)	L_A	1.5059 ± 0.0019		
Luminosity of B ($L_\odot$)	L_B	0.4981 ± 0.0007		

determined the orbital parameters (Keplerian orbital elements, dynamical parallax, total mass of the system, and mass ratio) for epoch 2019.5 based only on the RV and differential astrometry data and a simple Keplerian two-body model. In a second step, we adopted the dynamical parallax and mass ratio to determine the barycentric proper motion from the absolute Hipparcos and ALMA absolute astrometric positions of α Cen A and B. The position of the barycenter of the system was thus computed for each of the Hipparcos and ALMA measurement epochs. The space velocity of the barycenter of the AB system was then determined from this set of barycenter positions through a linear fit. For both steps, the determination of the best-fit parameters was obtained using a classical multi-parameter Levenberg–Marquardt least-squares fitting algorithm on the complete data set. It is based on the `scipy.optimize.leastsq` routine of the SciPy[7] library.

Among binary stars, α Cen is peculiar due to its proximity to the Earth and fast motion across the sky. As a consequence, we implemented in our orbital and proper motion model a few second-order corrective terms that have an influence on the orbital parameters and proper motion estimates. First, the very fast motion of α Cen induces a significant change in perspective of its space velocity vector (that comprises the RV and tangential velocity components). This geometrical effect has been known for decades (see, e.g., van de Kamp 1977), but to our knowledge it was not taken into account in recent computations of the orbital parameters of the system. It affects the barycentric RV and the tangential proper motion, both changing with time. The RV geometrically increases with an acceleration of $\dot{V} = +0.421$ m s^{-1}yr^{-1}, while the tangential velocity conversely decreases with time.

Another effect of the space motion of α Cen is a perspective-induced change of the inclination of the orbit as seen from the Earth. This creates a time-dependent variation of the apparent relative position of B with respect to A. In addition, as the distance to the Earth is presently decreasing, the apparent separation of the two stars is increasing. At the Hipparcos epoch (1991.25) the perspective change results in a shift in relative position of B compared to epoch 2019.5 of approximately 30 mas, which is not completely negligible compared to the error bars.

We also corrected the differential and absolute astrometric measurements for the light time propagation effect, based on our initial estimates of the barycentric RV. Due to the ≈ -22 km s^{-1} approach velocity of the system, the light time aberration on its apparent position on the sky is evolving, compared to our 2019.5 reference epoch. In other words, as α Cen was farther from the Earth in the past, its apparent position was slightly more "lagging behind" on its trajectory compared to its true position in space than it is today.

For these different second-order effects (perspective, light time), the changes are slow and can be considered linear over decades or even centuries. For this reason, we took them into account as a perturbation to our input data set. In practice, we computed an initial fit of the data without accounting for the perspective and light time effects. This resulted in an initial estimate of a mean value of the barycentric parallax, radial velocity, and proper motion vector. Based on these results, we corrected the input differential and absolute astrometric positions as well as the RV values of the two stars to bring them to our reference epoch of 2019.5. This reference time was arbitrarily chosen to correspond to the majority of our ALMA measurements, in order to limit the correlations between the proper motion vector components. For these computations, we extensively used the `SkyCoord` class and celestial coordinate system transformation routines available in the `Astropy`[8] library. We then computed a second round of orbital and proper motion fitting on these corrected observations, to determine the actual orbital parameters valid for our 2019.5 reference epoch. We checked that a third iteration of fitting did not result in a significant change of the derived parameters.

Finally, we emphasize that a complete astrometric solution is critical to removing the effects of the motions of α Cen A and B individually and as a system before looking for differential

[7] https://scipy.org

[8] https://www.astropy.org

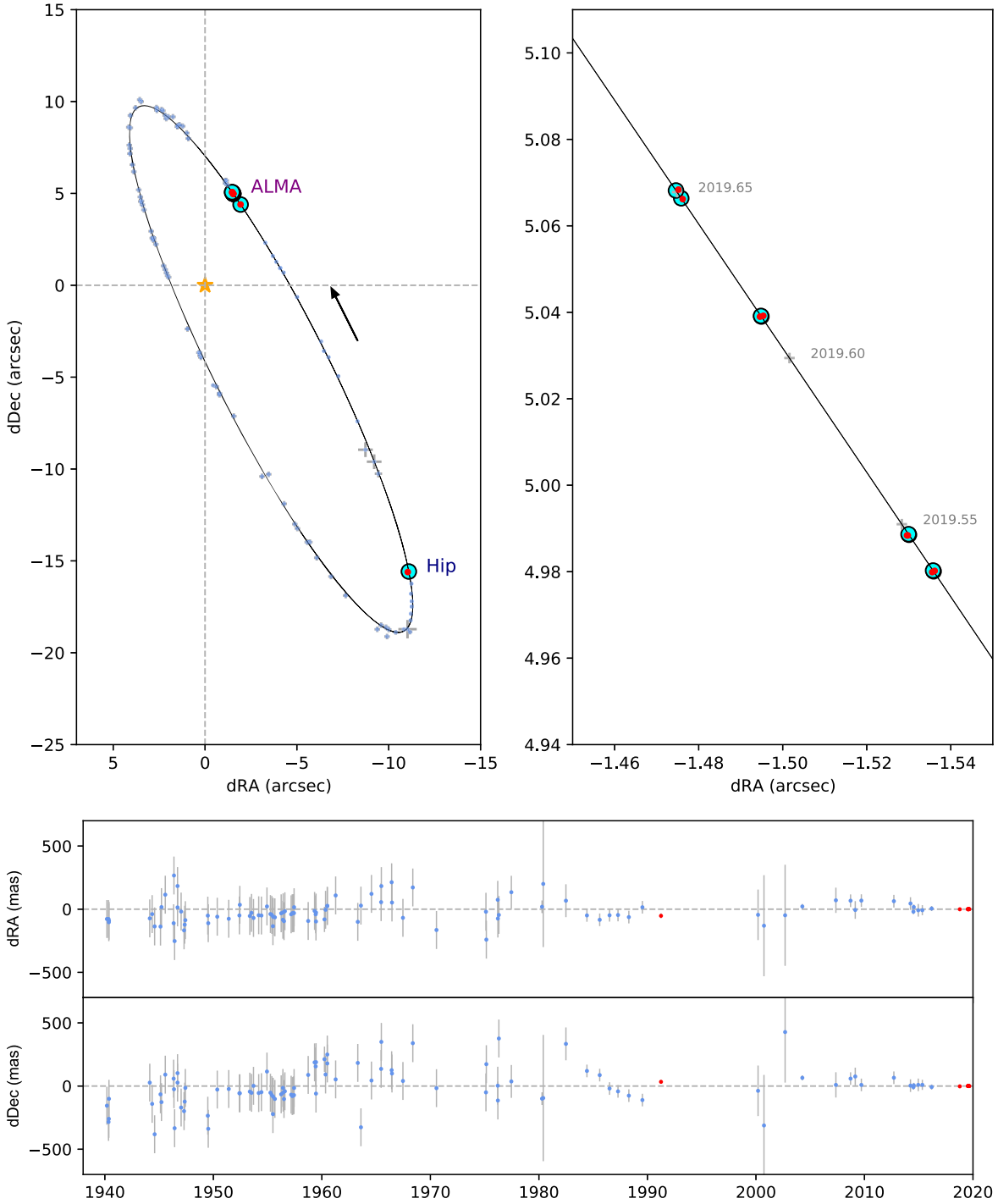

Figure 4. Top left panel: astrometric measurements and best-fit orbit of α Cen B relative to α Cen A. The red dots represent the Hipparcos and ALMA data, while the light blue dots show the other measurements. Top right panel: enlargement of the 2019 ALMA measurements. In both panels, the cyan disks represent the model positions corresponding to the Hipparcos and ALMA points. Bottom panels: residuals of the fit in R.A. and decl. as a function of time.

motions due to a planet. The 30 yr temporal baseline from Hipparcos and ALMA and the high precision of the example 5 yr observing ALMA program discussed in Section 3.3 would allow us to de-trend the effects of the 80 yr α Cen AB orbit to identify the short period signatures of planets at the tens of μas level in a $\sim$1 yr orbit (Section 3.2).

3.1.4. Orbital Parameters, Masses, and Barycentric Proper Motion

We list the best-fit orbital parameters and masses of the α Cen AB system in Table 8, and present the corresponding orbital trajectory in Figure 4. We obtain a satisfactory reduced χ^2 for the best-fit orbit model of 1.2. The radii are computed adopting the limb-darkened angular diameters measured by Kervella et al. (2017a). The luminosities of A and B are computed adopting the bolometric flux by Boyajian et al. (2013) and $L_{\odot} = 3.828 \times 10^{26}$ W.

We note differences between the Table 8 parallax and previous parallax determinations from Pourbaix & Boffin (2016, hereafter PB16) and Kervella et al. (2016, hereafter K16). The main differences between these past

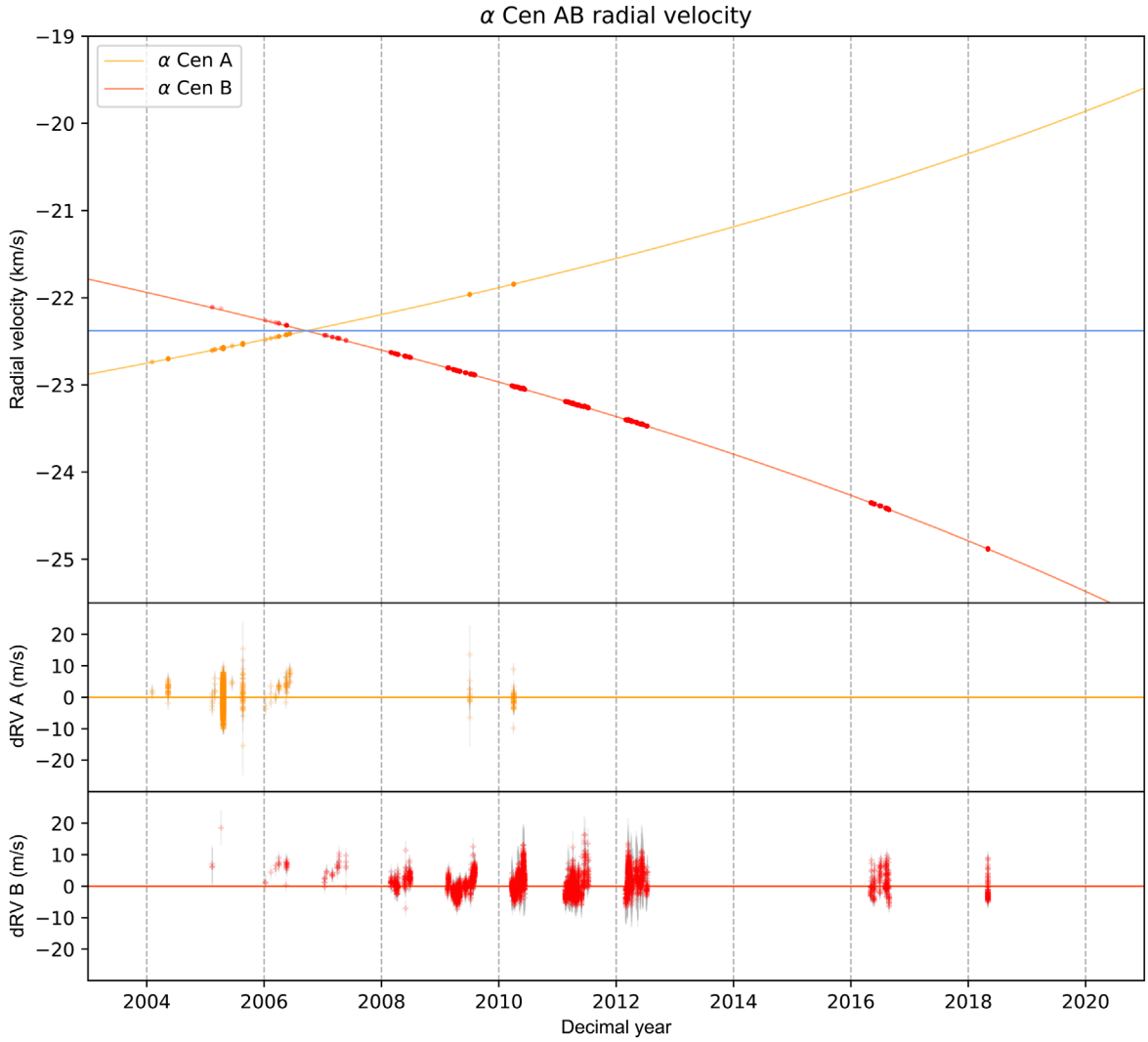

Figure 5. HARPS radial velocity data compared to the best-fit orbital model as a function of time (top panel) and residuals of the fit for α Cen A (middle panel) and B (bottom panel).

analyses and the present work includes the selection of the RV data set and our new high-accuracy ALMA differential astrometry. The radial velocity data used and the residuals of the fit are shown in Figure 5. The acquisition of new RV measurements with HARPS, particularly of α Cen A, would certainly improve the orbital phase coverage. We plot the residuals of the Hipparcos and ALMA absolute astrometric measurements to the best-fit orbit in Figure 6.

Table 9 lists the position and proper motion of the barycenter of the α Cen system for epoch 2019.5. The reduced χ^2 of the best-fit barycenter proper motion vector model is 1.6. For all of the model fitting done for the present work, the uncertainties of the best-fit parameters are normalized to the data dispersion around the best-fit model. In practice, this means that the 1σ uncertainties of the derived parameters are scaled by a factor of $\approx\sqrt{1.6}$. Through this rescaling, we take into account in the uncertainties the residual dispersion of the data points with respect to the model, which may be induced by instrumental or astrophysical effects.

Due to the perspective acceleration, the proper motion vector, together with the radial velocity, changes with time. The sky trajectory of α Cen A, B, and their barycenter is shown in Figure 7. The apparent motion of A and B is the result of the combination of the proper motion of the barycenter, orbital motion of the two components, and the parallax. Figure 8 displays the measured position of the AB barycenter compared to the parallactic ellipse derived from the orbital fit. Although the agreement is satisfactory between the measurements and the ellipse, this is not a fit. It is possible to derive the trigonometric parallax by fitting the observed Hipparcos and ALMA positions of the barycenter. But, due to relatively poor phase coverage of the parallactic ellipse because of our limited number of absolute measurements, the accuracy of the best-fit trigonometric parallax ($\varpi_{\rm trig} = 747.1 \pm 5.2$ mas) is significantly worse than that of the orbital parallax ($\varpi_{\rm orb} = 750.81 \pm 0.38$ mas). Both values are, however, statistically consistent.

3.2. Prospects for Improved Stellar Properties

The α Cen AB system is a touchstone for stellar astrophysics because these two stars straddle the Sun in mass with similar age, activity level, and metallicity. Because their physical properties can be determined with great precision due to their proximity to us, these stars are used for validation of stellar models and to check the predictions of techniques

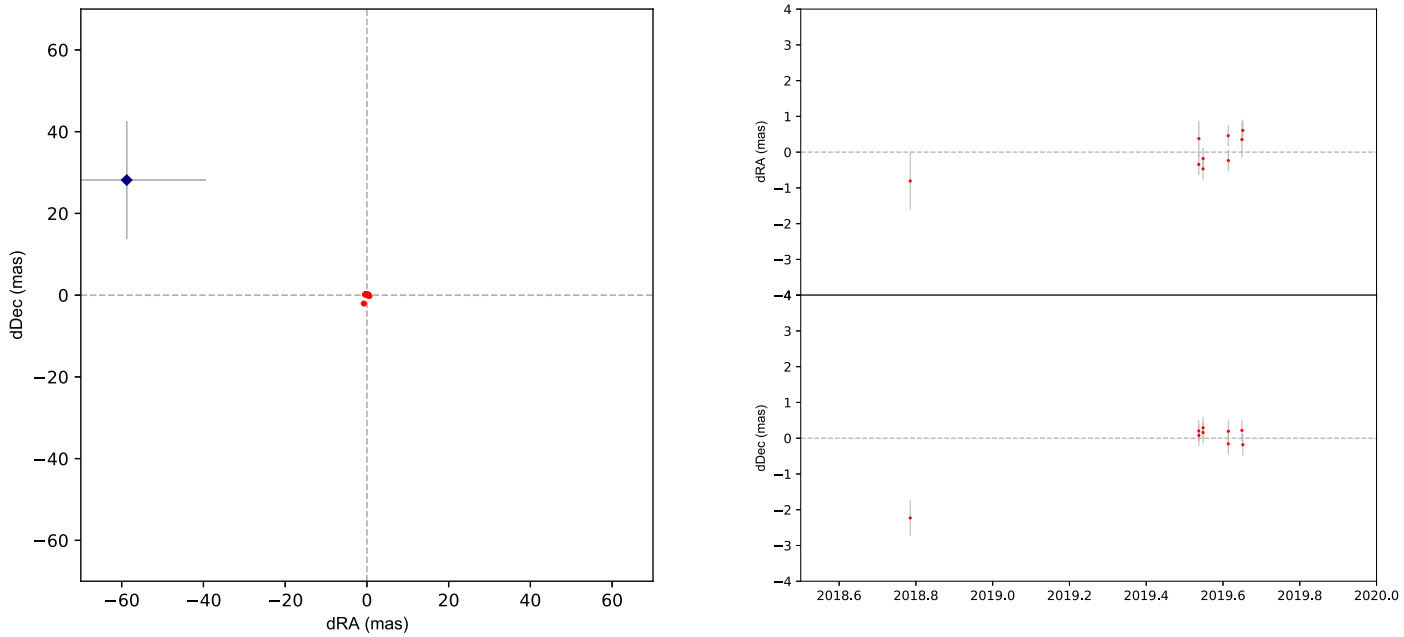

Figure 6. Left panel: differential position residuals of the ALMA (red) and Hipparcos (blue) measurements compared to the orbital fit of α Cen B relative to α Cen A on sky. Right panel: R.A. and decl. residuals of the ALMA differential A–B astrometric measurements with respect to the best-fit orbit, as a function of time.

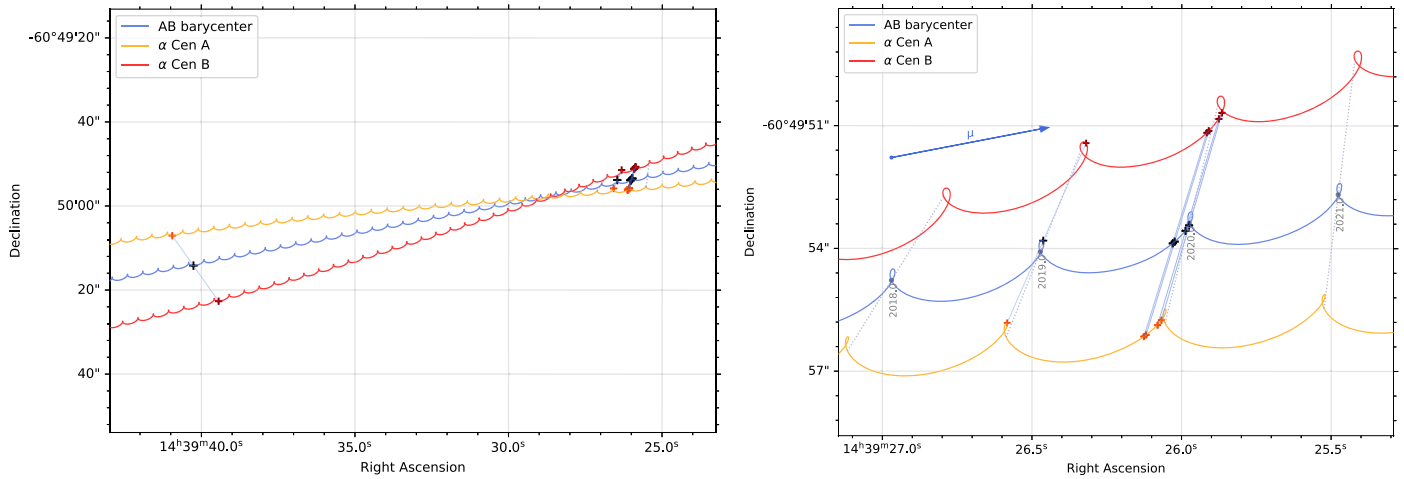

Figure 7. Sky trajectory of α Cen A, B and their barycenter, showing the Hipparcos and ALMA measurements (left panel) and an enlargement of the ALMA measurements (right panel). The individual points are shown with "+" symbols. The μ vector represents the annual proper motion of the barycenter.

Table 9
Position and Proper Motion (PM) of the Barycenter of α Cen A and B

Parameter		Present work (J2019.5)	K16, K17 (J1991.25)
RA (ICRS)	α_0	14:39:26.1413±1.50 mas	14:39:40.2068±25 mas
		$219.85892215 \pm 8.6\ 10^{-7}$ deg	…
Decl. (ICRS)	δ_0	−60:49:53.875±1.17 mas	−60:50:13.673±19 mas
		$-\ 60.83163195 \pm 3.3\ 10^{-7}$ deg	…
PM R.A. (mas yr^{-1})	μ_α	-3639.95 ± 0.42	-3619.9 ± 3.9
PM Decl. (mas yr^{-1})	μ_δ	$+700.40 \pm 0.17$	$+693.8 \pm 3.9$

Note. The parameters derived by Kervella et al. (2016, 2017b) are listed in the K16, K17 column for comparison.

such as asteroseismology (e.g., Joyce & Chaboyer 2018; Nsamba et al. 2019).

Alpha Cen is one of the Gaia mission benchmark systems selected as references for the determination of stellar parameters (Heiter et al. 2015). In advance of those anticipated, possibly more precise results, we discuss briefly how our new ALMA measurements improve the precision of our knowledge of α Cen A and B.

The combination of asteroseismic frequencies and interferometric radius measurements has proven to powerfully constrain

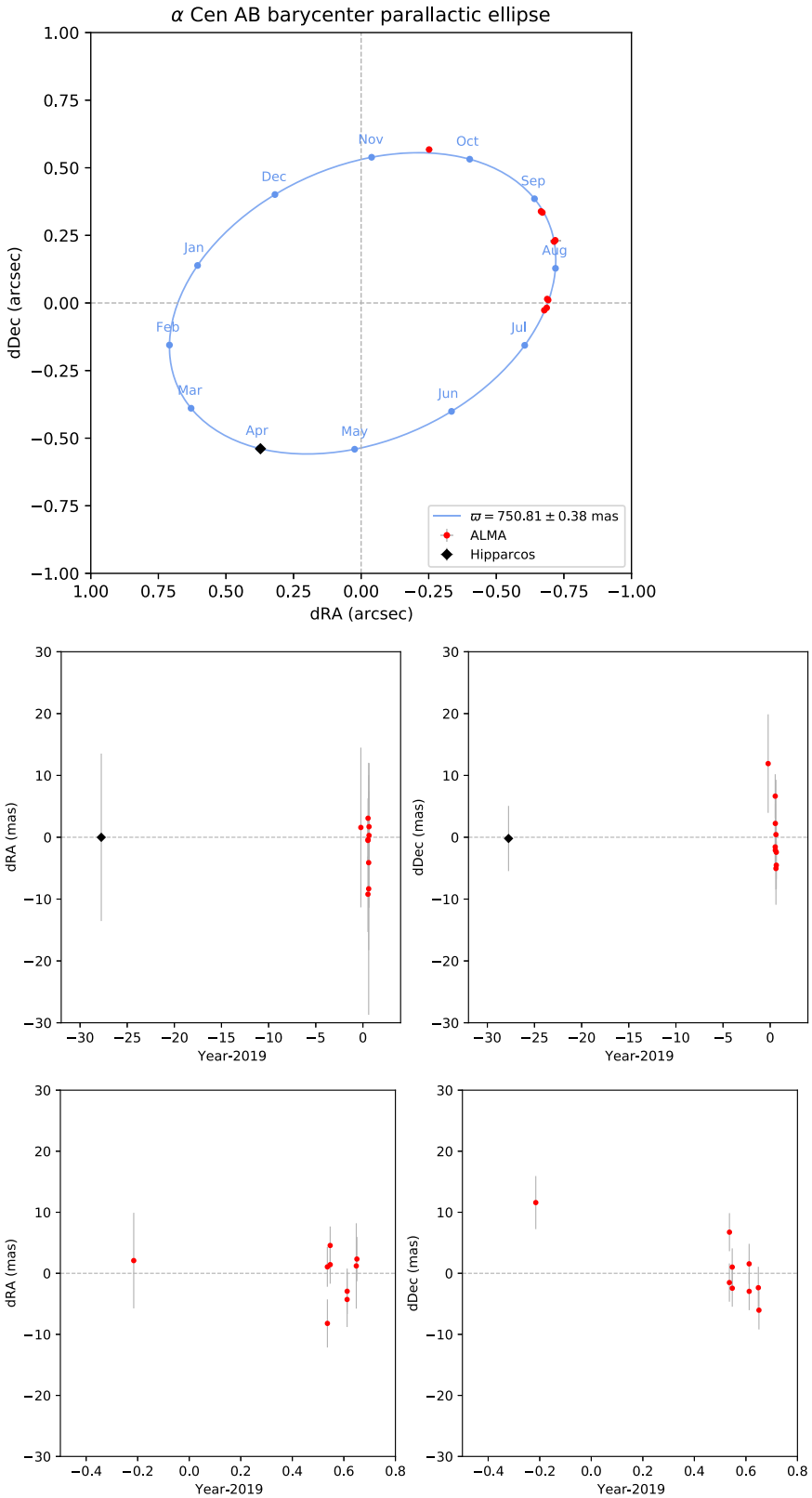

Figure 8. Top panel: positions of the barycenter of α Cen AB measured with ALMA (red) and Hipparcos (black) on the parallactic ellipse of α Cen (the proper motion has been subtracted). The ellipse corresponds to the parallax derived from the AB orbital fit (this is not a fit). Middle panels: residual positions of the barycenter of α Cen AB measured with Hipparcos (black) and ALMA (red points), compared to the best-fit trajectory including proper motion and parallax. Bottom panels: enlargement of the residuals of the ALMA measurements in 2018 and 2019 (red points).

the internal structure of stars (Cunha et al. 2007; Chaplin & Miglio 2013). Alpha Cen A and B were among the first stars to have their oscillation spectra measured with high precision by Bouchy & Carrier (2001, 2002), using radial velocity measurements with the CORALIE spectrograph. The angular diameters of α Cen A and B were first measured

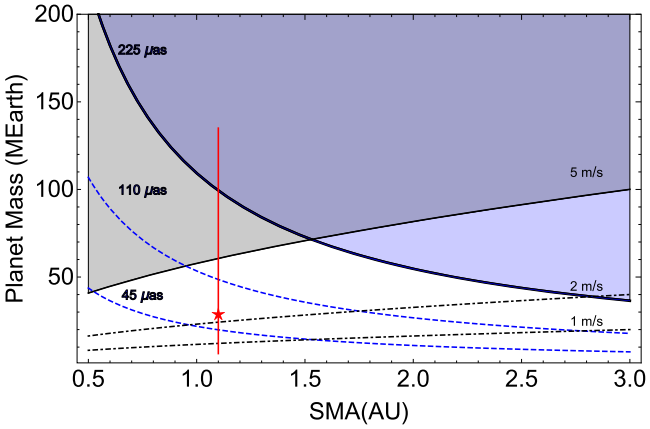

Figure 9. The sensitivity of astrometry and radial velocity measurements to planets in the semimajor axis (SMA)—planet mass plane for three different levels of precision for each technique (PRV in dotted–dashed black lines and ALMA astrometry in dashed blue lines). In each case we assume 2σ limits as described in the text. The red line and star denote the SMA and range of masses corresponding to the candidate planet detected by the VLT NEAR project (Kasper et al. 2019; Wagner et al. 2021).

Table 10
Orbital Parameters of Proxima Centauri

Parameter	Value	Unit
Semimajor axis a	$8.2^{+0.4}_{-0.3}$	kAU
Eccentricity e	$0.497^{+0.057}_{-0.060}$	
Period P	511^{+41}_{-30}	kyr
Inclination i	$124.9^{+2.9}_{-3.2}$	deg
Longitude of asc. node Ω	165^{+3}_{-3}	deg
Argument of periastron ω	$151.0^{+5.7}_{-4.9}$	deg
Epoch of periastron T_0[a]	$+278^{+36}_{-28}$	kyr
Periastron radius	$4.1^{+0.7}_{-0.6}$	kAU
Apastron radius	$12.3^{+0.2}_{-0.1}$	kAU

Note.
[a] The epoch of periastron passage T_0 is relative to present.

Table 11
Conjunctions of α Cen AB until 2031 with Background Stars S1 to S6 Identified by Kervella et al. (2016; their Table 3)

α Cen	$\rho_{\rm min}$ (arcsec)	Star	ΔV (mag)	Date	Date (decimal year)
B	0.088 ± 0.131	S01	18.7	2021 Apr 20	2021.301
A	1.509 ± 0.002	S02	15.7	2023 Apr 13	2023.279
B	1.484 ± 0.074	S03	18.4	2023 Dec 12	2023.946
B	2.283 ± 0.004	S04	16.2	2024 Oct 26	2024.818
A	0.170 ± 0.131	S05	21.5	2028 Apr 20	2028.301
B	0.294 ± 0.006	S06	15.6	2031 May 23	2031.389

Note. The minimum separation $\rho_{\rm min}$, closest approach date, and ΔV magnitude (from K16) are listed.

interferometrically with the VLTI/VINCI instrument by Kervella et al. (2003), and later refined with the VLTI/PIONIER instrument (Kervella et al. 2017a) at $\theta_{\rm LD}({\rm A}) = 8.502 \pm 0.038$ mas and $\theta_{\rm LD}({\rm B}) = 5.999 \pm 0.025$ mas. The parallax determined in the present work ($\varpi = 750.81$ mas, $d = 1.3319 \pm 0.0007$ pc) is larger by 0.49% compared to the value previously determined by Kervella et al. (2016; $\varpi = 747.17$ mas). As a result, we revise the linear radii of the two stars to $R_{\rm A} = 1.2175 \pm 0.0055\,R_\odot$ and $R_{\rm B} = 0.8591 \pm 0.0036\,R_\odot$, a change of approximately -1σ. The masses and radii values are close to the theoretical values determined by Thévenin et al. (2002) and Yildiz (2008) from the analysis of the asteroseismic frequencies of the two stars.

The determination of the age of stars is generally a complex enterprise (Soderblom 2010). In spite of the similarity of the physical properties of α Cen with the Sun and their well-determined masses, the estimate of their age (Mamajek & Hillenbrand 2008; Morel 2018; Sahlholdt et al. 2019), core properties (de Meulenaer et al. 2010; Bazot et al. 2016), and inner opacity (Yildiz 2011) remain a challenging task. For the evolutionary modeling of α Cen A and B, the treatment of convection is problematical, and the mixing-length parameter remains relatively uncertain (e.g., Yildiz 2007; Trampedach et al. 2014; Joyce & Chaboyer 2018; Spada & Demarque 2019).

For α Cen A and B, further progress on the modeling of structure and evolutionary status requires improvements to fundamental stellar parameters, both in higher precision and accuracy. Joyce & Chaboyer (2018) give the age of α Cen AB as 5.3 ± 0.3 Gyr based on masses that are $\sim$3% higher than those presented here. New models using these more precise values may result in revised ages for this touchstone system. While the uncertainties in the ages derived from the model fitting due to uncertainties in mixing length, etc., may remain the same, the centroid of the age estimates may shift significantly, especially as future ALMA observations reduce the parallax uncertainties by another factor of 2–3.

3.3. Prospects for Planet Detection Based on Differential Astrometry

Astrometric and PRV measurements have complementary selection biases. Astrometry favors planets more distant from the host star, and PRV planets closer in. Figure 9 shows limits to planets in the planet mass versus semimajor axis plane for the two techniques, each shown with three plausible levels of limiting sensitivity. PRV limits currently have a $\sim 2\sigma$ value of 5 m s^{-1} (Zhao et al. 2018), which we show potentially improving to 2 and 1 m s^{-1}. For the ALMA-based astrometry we adopt three cases based on a single measurement accuracy of 500, 250, and 100 μas and a series of 20 observations spread over 5 yr. The ALMA data presented here demonstrate a differential astrometric accuracy at the 300 μas level for our longest baseline configuration, that improves as expected with an increasing baseline length. The longest baselines available at ALMA are $\sim$2.5 times longer than the baselines used for the present observations, thus if the differential astrometry performance continues to scale with baseline length, single epoch observations at $\sim$100 μas are already feasible. To check our detection estimate, we compare with the astrometric data presented by Benedict & Harrison (2017). They used 31 Hubble Space Telescope Fine Guidance Sensor measurements, spanning 2.9 yr and having per observation a precision of 800 μas, to derive a semimajor axis of 760 ± 110 μas (2.4 au at 46 pc) for HD 202206c,a brown dwarf with a period of 3.45 yr, resulting in a $\sim 7\sigma$ detection. With a single measurement precision of $<$300 μas (Table 4), an ALMA campaign with a similar duration and cadence would yield a noise floor of $<$50 μas. A 20 observation campaign would have a slightly higher noise floor, $\sim$55 μas, or a two-sigma value of 110 μas,

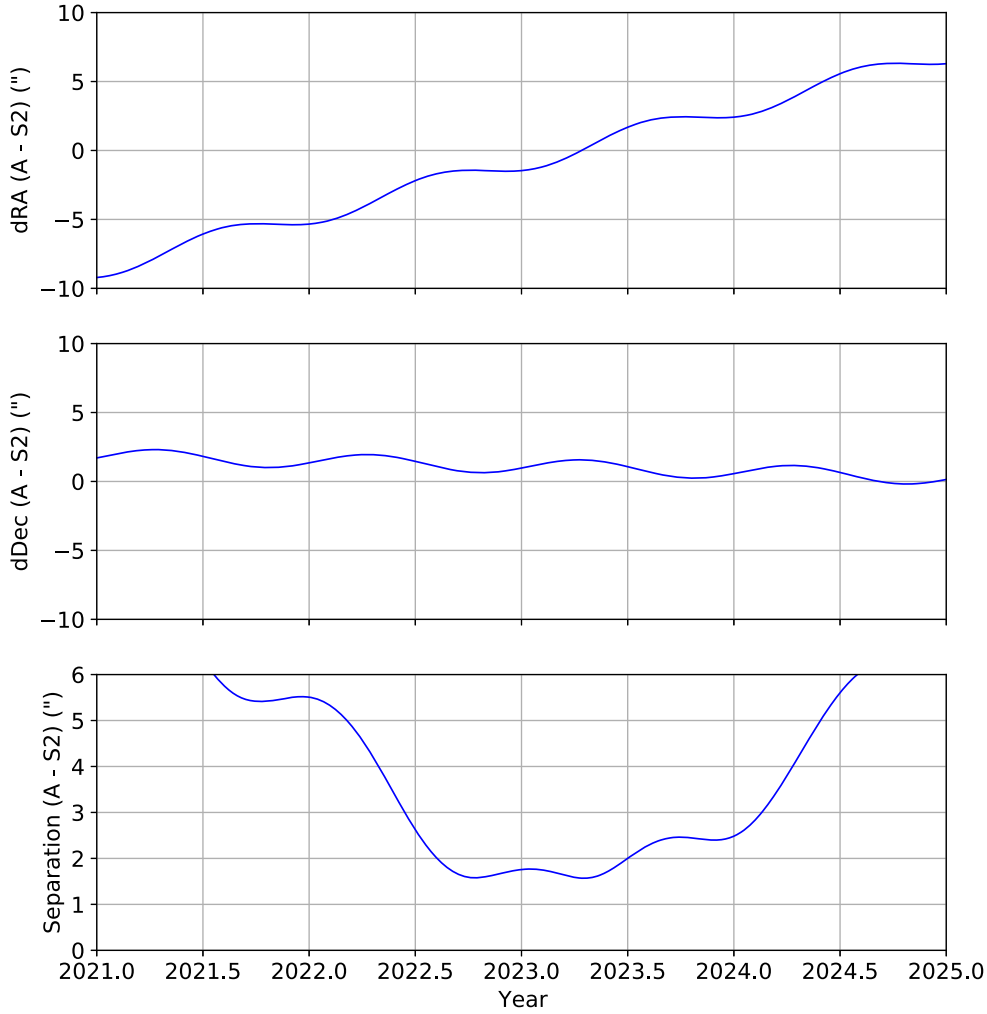

Figure 10. The trajectory of the star denoted S2 (Kervella et al. 2016) as it approaches α Cen A. The separation in R.A., decl., and total separation is shown as a function of time and incorporates the effects of proper motion, parallax, and orbital motion of α Cen A from this paper and the parallax and proper motion of S2 from Gaia.

and could lead to the identification of a 25 $M_\oplus$ planet with a 2 au orbital semimajor axis (Figure 9).

While such a program would be observationally challenging due to the ALMA configuration cycle, and a higher SNR would be needed for the detection of a planet in the absence of PRV data, ALMA astrometric data are clearly relevant in the exoplanet phase space of α Cen. When combined with PRV data, these complementary dynamical measurements will probe the entire 3 au region around each of the α Cen A and B components where planetary orbits are expected to be stable (Quarles & Lissauer 2016).

The mid-infrared direct imaging project NEAR (Kasper et al. 2019; Wagner et al. 2021) has tentatively identified a candidate planet associated with α Cen A. While instrument artifacts cannot yet be ruled out, they find an object at 1.1 au from α Cen A with a range of possible radii between 3.3 and 7 $M_\oplus$. Converting radius to mass is of course an uncertain process. Taking transiting planets in this radius range with masses measured with better than 20% accuracy[9], we find an average mass of 30 $M_\oplus$, a minimum mass of 6 $M_\oplus$, and a maximum mass of 135 $M_\oplus$. While existing measurements would seem to rule out the largest possible masses, future observations of either type could determine the mass of this putative object.

3.4. The Orbit of Proxima Centauri and α Cen AB Stellar Conjunctions

Our accurate determination of the barycentric parallax, radial velocity, and proper motion of α Cen AB (Tables 8 and 9) enables us to improve our knowledge of the relative velocity between the inner AB system and the third component of the system, Proxima Centauri (Kervella et al. 2017b). We adopt the Hipparcos–Gaia proper motion determined by Kervella et al. (2019) for Proxima ($\mu_\alpha = -3781.629 \pm 0.048$ mas a^{-1}; $\mu_\delta = +769.421 \pm 0.052$ mas a^{-1}) and the radial velocity from Kervella et al. (2017b; $v_{\rm r,abs} = -22.204 \pm 0.032$ km s^{-1}). The improved parallax and masses of the AB system translate into an unbound differential velocity limit of $v_{\rm max} = 554 \pm 7$ m s^{-1} for a gravitationally bound system. We obtain a differential space velocity of $\Delta v_{\alpha-{\rm Prox}} = 280 \pm 32$ m s^{-1} between α Cen AB and Proxima, very significantly below the unbound velocity. The significance of the gravitational link between AB and Proxima has therefore increased over the last three years from 4.4σ in Kervella et al. (2017b), to 5.5σ in Kervella et al. (2019), to 8.3σ in the present work ($<10^{-15}$ false alarm

[9] https://exoplanetarchive.ipac.caltech.edu/index.html (Akeson et al. 2013).

probability). Proxima becomes a yet more valuable check on lower main sequence stellar modeling. We list the refined parameters for the orbit of Proxima in Table 10.

Using the improved proper motion and orbital parameters of α Cen AB determined in the present work, it is possible to refine the predictions of the stellar conjunctions between α Cen AB and background field stars that were identified by K16. We took into account the positions and proper motions of stars S2, S4, and S6 (see Table 3; K16) that are listed in the Gaia DR3 catalog (Gaia Collaboration et al. 2021). For stars S1, S3, and S5, we adopted the uncertainties from K16, in particular an uncertainty on their proper motion of ± 10 mas yr^{-1}. Thanks to the new ALMA astrometry, the trajectory of α Cen AB is significantly better constrained, resulting in a significant reduction of the uncertainties on the conjunction parameters in particular the minimum approach angular separation $\rho_{\rm min}$ (Table 11). The trajectory of S2 is shown in Figure 10 with a closest approach to α Cen A of $1\farcs5$ in mid 2023. With $\Delta K = 12.6$ mag, S2 will provide a well-defined "test particle" for searches for Jovian-sized planets via infrared direct imaging experiments (Beichman et al. 2020).

For stars S1, S3, and S5, the error budget is dominated by the uncertainty on the position and proper motion of these field stars, and the error bars on $\rho_{\rm min}$ are only moderately improved compared to those in K16 (their Table 3). The revised $\rho_{\rm min}$ and dates of closest approach are generally close to the previously determined values, except for the S3 event in 2023 that occurs about six months earlier than calculated in K16.

4. Conclusions

1. We have demonstrated that ALMA produces for the nearby bright stars α Cen A and B absolute astrometric measures with a precision and accuracy of order 3 mas and differential separation uncertainties of 300 to 600 μas.
2. By comparison with the Sun we establish an astrometric jitter due to stellar activity of less than 15 μas.
3. The combination of historical measurements of the α Cen A–B position angle and separation, more recent PRV measurements from HARPS, and absolute astrometry from Hipparcos and ALMA yields improved α Cen A and B orbital elements, system proper motion and parallax, and component masses.
4. We find stellar parameters of $m_{\rm A} = 1.0788 \pm 0.0029\ M_\odot$ and $m_{\rm B} = 0.9092 \pm 0.0025\ M_\odot$, and $R_{\rm A} = 1.2175 \pm 0.0055\ R_\odot$ and $R_{\rm B} = 0.8591 \pm 0.0036\ R_\odot$. These masses and radii, now improved with a more precise and accurate parallax, will serve to further constrain stellar evolutionary models and provide "ground truth" for asteroseismological predictions.
5. Our accurate determination of the α Cen AB system parallax, RV, and proper motion, when compared to those values for Proxima Centauri, confirms that the three stars constitute a bound system.
6. Continued astrometric monitoring of the α Cen AB system with ALMA, particularly with longer baseline configurations and in combination with precision radial velocity measurements, should reduce planetary companion detection limits to the few tens of $M_\oplus$ range across the entire <3 au region expected to be stable in the α Cen AB system.

This paper makes use of the following ALMA data: ADS/JAO.ALMA #2018.1.00557.S. ALMA is a partnership of ESO (representing its member states), NSF (USA) and NINS (Japan), together with NRC (Canada), MOST and ASIAA (Taiwan), and KASI (Republic of Korea), in cooperation with the Republic of Chile. The Joint ALMA Observatory is operated by ESO, AUI/NRAO, and NAOJ. The National Radio Astronomy Observatory is a facility of the National Science Foundation operated under cooperative agreement by Associated Universities, Inc. Some of the research described in this publication was carried out in part at the Jet Propulsion Laboratory, California Institute of Technology, under a contract with the National Aeronautics and Space Administration. G.F.B. thanks McDonald Observatory for extending a Research Fellow position, allowing continued possession of an office and computing equipment. We thank the referees for a careful reading of the paper and for making many useful suggestions to clarify the material.

Facilities: ALMA, ESO:3.6 m(HARPS).

Software: CASA (McMullin et al. 2007), astropy (Astropy Collaboration et al. 2013, 2018).

Appendix A
Ephemeris of α Cen A and B

To help in the preparation of future observations of α Cen, we present in this section the coordinates of α Cen A and B as a function of time for the period between 2010 and 2050. Table 12 gives the positions of the AB center of mass, A, and B in the ICRS frame. These coordinates take into account the proper motion, orbital motion, and parallactic wobble of the two stars. The relative position of B with respect to A in Cartesian and spherical coordinates is also provided, and the evolution of the separation and position angle of α Cen B relative to A are shown in Figure 11.

Table 12
Ephemeris of α Cen A and B between 2010 and 2050

Date	R.A.$_{AB}$	Decl.$_{AB}$	R.A.$_{A}$	Decl.$_{A}$	R.A.$_{B}$	Decl.$_{B}$	dR.A. (arcsec)	dDecl. (arcsec)	ρ (arcsec)	θ (degrees)
2010.00	14:39:30.9533	−60:50:00.386	14:39:31.3371	−60:49:59.098	14:39:30.4978	−60:50:01.913	−6.136	−2.815	6.751	245.357
2010.05	14:39:30.9404	−60:50:00.527	14:39:31.3230	−60:49:59.259	14:39:30.4865	−60:50:02.032	−6.115	−2.774	6.715	245.600
2010.10	14:39:30.9180	−60:50:00.665	14:39:31.2992	−60:49:59.415	14:39:30.4656	−60:50:02.148	−6.094	−2.733	6.679	245.845
2010.15	14:39:30.8857	−60:50:00.782	14:39:31.2657	−60:49:59.551	14:39:30.4349	−60:50:02.243	−6.073	−2.692	6.643	246.093
2010.20	14:39:30.8445	−60:50:00.863	14:39:31.2231	−60:49:59.651	14:39:30.3953	−60:50:02.302	−6.052	−2.651	6.607	246.344
2010.25	14:39:30.7961	−60:50:00.897	14:39:31.1734	−60:49:59.704	14:39:30.3484	−60:50:02.313	−6.031	−2.610	6.571	246.598
2010.30	14:39:30.7429	−60:50:00.878	14:39:31.1189	−60:49:59.703	14:39:30.2968	−60:50:02.272	−6.010	−2.569	6.536	246.855
2010.35	14:39:30.6877	−60:50:00.805	14:39:31.0623	−60:49:59.649	14:39:30.2431	−60:50:02.176	−5.988	−2.528	6.500	247.114
2010.40	14:39:30.6334	−60:50:00.682	14:39:31.0067	−60:49:59.545	14:39:30.1904	−60:50:02.031	−5.967	−2.487	6.465	247.376
2010.45	14:39:30.5828	−60:50:00.519	14:39:30.9548	−60:49:59.400	14:39:30.1414	−60:50:01.846	−5.946	−2.446	6.429	247.641
2010.50	14:39:30.5382	−60:50:00.327	14:39:30.9089	−60:49:59.227	14:39:30.0984	−60:50:01.632	−5.925	−2.405	6.394	247.909
2010.55	14:39:30.5015	−60:50:00.121	14:39:30.8709	−60:49:59.040	14:39:30.0633	−60:50:01.404	−5.903	−2.364	6.359	248.180
2010.60	14:39:30.4739	−60:49:59.918	14:39:30.8418	−60:49:58.856	14:39:30.0372	−60:50:01.178	−5.882	−2.322	6.324	248.454
2010.65	14:39:30.4555	−60:49:59.733	14:39:30.8221	−60:49:58.689	14:39:30.0204	−60:50:00.971	−5.861	−2.281	6.289	248.730
2010.70	14:39:30.4459	−60:49:59.580	14:39:30.8112	−60:49:58.555	14:39:30.0124	−60:50:00.795	−5.839	−2.240	6.254	249.010
2010.75	14:39:30.4437	−60:49:59.471	14:39:30.8076	−60:49:58.466	14:39:30.0118	−60:50:00.665	−5.818	−2.199	6.219	249.294
2010.80	14:39:30.4468	−60:49:59.415	14:39:30.8094	−60:49:58.428	14:39:30.0165	−60:50:00.586	−5.796	−2.158	6.185	249.580
2010.85	14:39:30.4525	−60:49:59.413	14:39:30.8138	−60:49:58.445	14:39:30.0239	−60:50:00.562	−5.775	−2.117	6.150	249.869
2010.90	14:39:30.4579	−60:49:59.464	14:39:30.8178	−60:49:58.515	14:39:30.0308	−60:50:00.591	−5.753	−2.075	6.116	250.162
2010.95	14:39:30.4597	−60:49:59.560	14:39:30.8182	−60:49:58.629	14:39:30.0342	−60:50:00.663	−5.731	−2.034	6.082	250.458
2011.00	14:39:30.4552	−60:49:59.686	14:39:30.8124	−60:49:58.775	14:39:30.0314	−60:50:00.768	−5.710	−1.993	6.048	250.758
2011.05	14:39:30.4424	−60:49:59.827	14:39:30.7982	−60:49:58.935	14:39:30.0201	−60:50:00.887	−5.688	−1.952	6.014	251.061
2011.10	14:39:30.4199	−60:49:59.965	14:39:30.7744	−60:49:59.092	14:39:29.9993	−60:50:01.002	−5.666	−1.911	5.980	251.367
…										

Note. The R.A.$_{AB}$ and decl.$_{AB}$ columns correspond to the center of mass position. Parameters dR.A. and dDecl. are the position offsets of B relative to A, expressed in arcseconds, ρ is the A–B separation, and θ the position angle of B with respect to A ($N = 0$, $E = 90°$). These coordinates include the proper motion, orbital motion, and parallactic wobble of the two stars, and the light time propagation delay.

(This table is available in its entirety in machine-readable form.)

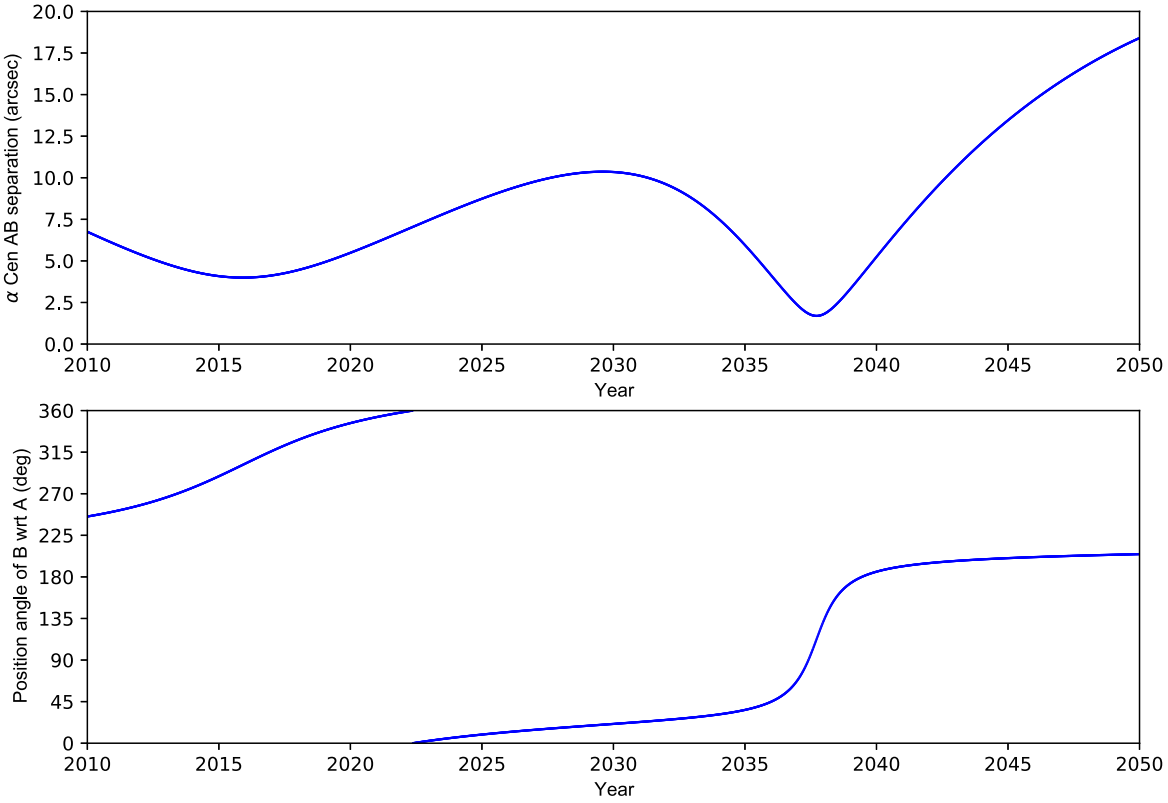

Figure 11. Apparent separation and position angle ($N = 0$, $E = 90°$) of α Cen B relative to A between 2010 and 2050.

ORCID iDs

Rachel Akeson https://orcid.org/0000-0001-9674-1564
Charles Beichman https://orcid.org/0000-0002-5627-5471
Pierre Kervella https://orcid.org/0000-0003-0626-1749
Edward Fomalont https://orcid.org/0000-0002-9036-2747
G. Fritz Benedict https://orcid.org/0000-0003-2852-3279

References

Akeson, R. L., Chen, X., Ciardi, D., et al. 2013, PASP, 125, 989
Anton, R. 2014, JDSO, 10, 232
Anton, R. 2015, JDSO, 11, 81
Astropy Collaboration, Price-Whelan, A. M., Sipőcz, B. M., et al. 2018, AJ, 156, 123
Astropy Collaboration, Robitaille, T. P., Tollerud, E. J., et al. 2013, A&A, 558, A33
Baraffe, I., Homeier, D., Allard, F., et al. 2015, A&A, 577, A42
Bazot, M., Christensen-Dalsgaard, J., Gizon, L., & Benomar, O. 2016, MNRAS, 460, 1254
Beichman, C., Ygouf, M., Llop Sayson, J., et al. 2020, PASP, 132, 015002
Benedict, G. F., & Harrison, T. E. 2017, AJ, 153, 258
Benedict, G. F., & McArthur, B. E. 2020, RNAAS, 4, 86
Boro Saikia, S., Marvin, C. J., Jeffers, S. V., et al. 2018, A&A, 616, A108
Bouchy, F., & Carrier, F. 2001, A&A, 374, L5
Bouchy, F., & Carrier, F. 2002, A&A, 390, 205
Boyajian, T. S., von Braun, K., van Belle, G., et al. 2013, ApJ, 771, 40
Chaplin, W., & Miglio, A. 2013, ARA&A, 51, 353
Cunha, M. S., Aerts, C., Christensen-Dalsgaard, J., et al. 2007, A&ARv, 14, 217
Curiel, S., Ortiz-León, G. N., Mioduszewski, A. J., et al. 2020, AJ, 160, 97
de Meulenaer, P., Carrier, F., Miglio, A., et al. 2010, A&A, 523, A54
Dumusque, X. 2018, A&A, 620, A47
Engels, D., Sherwood, W. A., Wamsteker, W., et al. 1981, A&AS, 45, 5
Gaia Collaboration, Brown, A. G. A., Vallenari, A., et al. 2021, A&A, 649, A1
Hartkopf, William I., Mason, Brian D., & Worley, Charles E. 2001, AJ, 122, 3472
Heiter, U., Jofré, P., Gustafsson, B., et al. 2015, A&A, 582, A49
Holman, M. J., & Wiegert, P. A. 1999, AJ, 117, 621
Joyce, M., & Chaboyer, B. 2018, ApJ, 864, 99
Kasper, M., Arsenault, R., Käufl, U., et al. 2019, Msngr, 178, 5
Kervella, P., Arenou, F., Mignard, F., & Thévenin, F. 2019, A&A, 623, A72
Kervella, P., Arenou, F., & Schneider, J. 2020, A&A, 635, L14
Kervella, P., Bigot, L., Gallenne, A., et al. 2017a, A&A, 597, A137
Kervella, P., Mignard, F., Mérand, A., & Thévenin, F. 2016, A&A, 594, A107
Kervella, P., Thévenin, F., & Lovis, C. 2017b, A&A, 598, L7
Kervella, P., Thévenin, F., Ségransan, D., et al. 2003, A&A, 404, 1087
Liseau, R. 2019, arXiv:1904.03043
Liseau, R., De la Luz, V., O'Gorman, E., et al. 2016, A&A, 594, A109
Liseau, R., Montesinos, B., Olofsson, G., et al. 2013, A&A, 549, L7
Liseau, R., Vlemmings, W., Bayo, A., et al. 2015, A&A, 573, L4
Lisogorskyi, M., Jones, H. R. A., & Feng, F. 2019, MNRAS, 485, 4804
Makarov, V. V., Beichman, C. A., Catanzarite, J. H., et al. 2009, ApJL, 707, L73
Mamajek, E. E., & Hillenbrand, L. A. 2008, ApJ, 687, 1264
McMullin, J. P., Waters, B., Schiebel, D., et al. 2007, adass XVI, 376, 127
Mezger, P. G., & Henderson, A. P. 1967, ApJ, 147, 471
Monet, D. G., Jenkins, J. M., Dunham, E. W., et al. 2010, arXiv:1001.0305
Morel, T. 2018, A&A, 615, A172
Nsamba, B., Campante, T. L., Monteiro, M. J. P. F. G., et al. 2019, FrASS, 6, 25
Pourbaix, D., & Boffin, H. M. J. 2016, A&A, 586, A90
Pourbaix, D., Nidever, D., McCarthy, C., et al. 2002, A&A, 386, 280
Quarles, B., & Lissauer, J. J. 2016, AJ, 151, 111
Quarles, B., & Lissauer, J. J. 2018, AJ, 155, 130
Quarles, B., Lissauer, J. J., & Kaib, N. 2018, AJ, 155, 64
Robrade, J., & Schmitt, J. H. M. M. 2016, arXiv:1612.06570
Sahlholdt, C. L., Feltzing, S., Lindegren, L., & Church, R. P. 2019, MNRAS, 482, 895
Schwab, F. R. 1980, Proc. SPIE, 231, 18
Shibasaki, K. 2013, PASJ, 65, S17
Soderblom, D. 2010, ARA&A, 48, 581
Spada, F., & Demarque, P. 2019, MNRAS, 489, 4712
Thévenin, F., Provost, J., Morel, P., et al. 2002, A&A, 392, L9
Trampedach, H., Stein, R. F., Christensen-Dalsgaard, J., et al. 2014, MNRAS, 445, 4366

Trifonov, T., Tal-Or, L., Zechmeister, M., et al. 2020, A&A, 636, A74
Trigilio, C., Umana, G., Cavallaro, F., et al. 2018, MNRAS, 481, 217
van de Kamp, P. 1977, VA, 21, 289
van Leeuwen, F. 2007, Hipparcos, the New Reduction of the Raw Data: Astrophysics and Space Science Library, 350 (Berlin: Springer)
Wagner, K., Boehle, A., Pathak, P., et al. 2021, NatCo, 12, 922
Yildiz, M. 2007, MNRAS, 374, 1264
Yildiz, M. 2008, MNRAS, 388, 1143
Yildiz, M. 2011, MNRAS, 412, 2571
Zhao, L., Fischer, D. A., Brewer, J., et al. 2018, AJ, 155, 24